The Cryosphere Discuss., 8, 3699–3732, 2014
www.the-cryosphere-discuss.net/8/3699/2014/
doi:10.5194/tcd-8-3699-2014

The Cryosphere Discussions
Open Access

Regional albedo of Arctic first-year drift ice in advanced stages of melt from the combination of in situ measurements and aerial imagery

D. V. Divine, M. A. Granskog, S. R. Hudson, C. A. Pedersen, T. I. Karlsen, S. A. Divina, and S. Gerland

Norwegian Polar Institute, FRAM Centre, 9296 Tromsø, Norway

Received: 17 June 2014 – Accepted: 22 June 2014 – Published: 11 July 2014

Correspondence to: D. V. Divine (dmitry.divine@npolar.no)

Published by Copernicus Publications on behalf of the European Geosciences Union.

Abstract

The paper presents a case study of the regional (≈ 150 km) broadband albedo of first year Arctic sea ice in advanced stages of melt, estimated from a combination of in situ albedo measurements and aerial imagery. The data were collected during the eight day ICE12 drift experiment carried out by the Norwegian Polar Institute in the Arctic north of Svalbard at 82.3° N from 26 July to 3 August 2012. The study uses in situ albedo measurements representative of the four main surface types: bare ice, dark melt ponds, bright melt ponds and open water. Images acquired by a helicopter borne camera system during ice survey flights covered about 28 km^2. A subset of > 8000 images from the area of homogeneous melt with open water fraction of ≈ 0.11 and melt pond coverage of ≈ 0.25 used in the upscaling yielded a regional albedo estimate of 0.40 (0.38; 0.42). The 95 % confidence interval on the estimate was derived using the moving block bootstrap approach applied to sequences of classified sea ice images and albedo of the four surface types treated as random variables. Uncertainty in the mean estimates of surface type albedo from in situ measurements contributed some 95 % of the variance of the estimated regional albedo, with the remaining variance resulting from the spatial inhomogeneity of sea ice cover. The results of the study are of relevance for the modeling of sea ice processes in climate simulations. It particularly concerns the period of summer melt, when the optical properties of sea ice undergo substantial changes, which existing sea ice models have significant diffuculty accurately reproducing.

1 Introduction

A new thin-ice Arctic system requires reconsideration of the set of parameterizations of mass and energy exchange within the ocean–sea ice–atmosphere system used in modern coupled general circulation models (CGCMs) including Earth System Models (ESMs). Such a reassessment would require a comprehensive collection of measure-

TCD
8, 3699–3732, 2014

ments made specifically on first-year pack ice with a focus on the summer melt season, when the difference from typical conditions for the earlier multi-year Arctic sea ice cover becomes most pronounced (Perovich and Polashenski, 2012).

Surface albedo is one of the major physical quantities controlling the intensity of the energy exchange at the atmosphere–sea ice–ocean interface and the heat balance of sea ice (e.g. Doronin and Kheisin, 1977; Maykut, 1982; Curry et al., 1995). Knowledge of the surface albedo for different types of sea ice, as well as its spatial and seasonal variability, is crucial for obtaining an adequate representation of the sea-ice cycle in CGCMs (Holland et al., 2012; Karlsson and Svensson, 2013).

During summer, the net positive heat balance of sea ice causes substantial transformation in the state of the ice cover. Water runoff from melting snow and upper ice layers tends to form puddles in depressions in the sea ice surface (e.g. Zubov, 1945; Untersteiner, 1961; Nazintsev, 1964). These melt ponds spread rapidly and on level first year ice can cover up to 70 % of the surface during the initial stage of surface melt (Polashenski et al., 2012). As the albedo of a melt pond is markedly lower than that of the bare or snow-covered sea ice (e.g. Doronin and Kheisin, 1977; Perovich et al., 2002), the spatial distribution of melt ponds and leads has clear implications for the spatial aggregate albedo and accelerated summer decay of sea ice.

Field observations suggest a pronounced difference in the seasonal evolution of first-year sea-ice albedo compared with that of multiyear ice. The surface of multiyear sea ice typically features more rough topography and thicker snow cover, leading to a limited potential melt pond coverage (e.g. Perovich and Polashenski, 2012). Thicker ice underneath the melt pond bottom leads to generally higher spatial albedo, lower transmission and energy absorption of melting multiyear ice (Hudson et al., 2013; Nicolaus et al., 2012). As a result, the summer albedo of multiyear ice cover is systematically higher than that of younger ice throughout the entire melt season, inducing an additional ice age–albedo feedback (Perovich and Polashenski, 2012).

The relatively small spatial scale of a typical pond system (typically few hundreds to thousands of m^2, e.g. Hohenegger et al., 2012), large intersite variability in melt

TCD
8, 3699–3732, 2014

pond coverage, and the overcast conditions prevailing in the summer Arctic promote the use of low-altitude airborne methods for studying the morphological and optical properties of the sea ice cover. Combining these with in situ measurements of incident/reflected solar radiation (albedo) and turbulent heat fluxes for different types of surfaces may in turn provide estimates of the regional-scale surface energy balance of sea ice. A number of such studies have been conducted in the past with a focus on spatial and temporal evolution of fractional melt pond coverage, pond-size probability density (see e.g. Perovich et al., 2002 for a review), and their relationship with the pre-melt surface topography (Derksen et al., 1997; Petrich et al., 2012). Depending on the instrumentation setup used, the spatial ranges covered varied from tens of meters to hundreds of kilometers, on the order of the typical scale of a GCM grid cell.

A comprehensive set of observations of the energy balance of melting Arctic first-year sea ice was conducted during an eight-day ice station in July–August 2012. Hudson et al. (2013) presented results from in situ measurements obtained during the drift experiment. This paper shows the analysis of the regional morphological properties of the sea-ice surface, inferred from aerial surveys. The in situ measurements of broadband albedo and the derived regional spatial distribution of surface types are used to obtain an estimate of the regional albedo of Arctic first-year ice in the advanced stages of melt.

Section 2 presents the geographical settings, instrument setup, image processing techniques used in the study, and uncertainties in the key variables we used for estimating the regional albedo. Section 3.1 shows the spatial variability of melt pond and open water fractions inferred from six helicopter ice survey flights. Details on the upscaling technique applied, along-track albedo variability, and regional albedo estimates are then presented in Sect. 3.2. Finally the results of the work are discussed and summarized in Sect. 4.

TCD
8, 3699–3732, 2014

2 Data and methods

2.1 ICE12 drift experiment

The energy balance of melting thin first-year Arctic sea ice was a focus of the eight-day ICE12 drifting ice floe experiment on R/V *Lance*, conducted 26 July to 3 August 2012 north of Svalbard, in the southwestern Nansen Basin (82.3° N, 21.5° E). Figure 1 shows the *Lance* drift track that was in an area of very close (≥ 90 %) drift ice, see operational ice charts from the Norwegian Ice Service for reference (www.met.no). The ice floe (ICE12 floe hereafter) that *Lance* was moored to during the drift had a size of approximately ⌀ 600 m and a modal ice thickness of 0.8 m, from drillings and measurements using a Geonics EM-31 electromagnetic induction device (Hudson et al., 2013). Based on airborne surveys of ice thickness using another electromagnetic induction device, the EM-bird (Haas et al., 2009), and aerial photography, it was found to be representative for the area. The sea ice was in the latter stages of melt, with some of the ponds actually melted through the ice slab.

The imaging of the sea-ice surface during the cruise was done using a recently designed ICE camera system mounted on a Eurocopter AS-350 helicopter. The hardware component of the system includes two downward looking Canon EOS 5D Mark II digital photo cameras equipped with Canon 20 mm f/2.8 USM lenses, a combined SPAN-CPT GPS/INS unit by Novatel, and a laser distance measurement device LDM301 by Jenoptik used as an altimeter in the setup. These components were housed in a single aerodynamic enclosure and mounted outside the helicopter. The single-point horizontal positioning accuracy for the system was within 1.5 m, and the uncertainty in the altitude over the sea ice was estimated to be < 0.3 m, which corresponds to a typical scale of sea ice draft variability.

Since the ICE camera was designed as a component of a photogrammetric setup, the image shooting rate was set to one frame per second per camera yielding two captured images per second. This was sufficient to ensure about 50–70 % overlap between successive images for flights at an altitude of 35–40 m and with a velocity of

TCD
8, 3699–3732, 2014

30–40 m s^{-1} – parameters typical for EM-bird flights. We fixed the camera lenses' focal lengths to infinity. For every captured image, the position, attitude, and altitude of the event were logged in the system. The cameras' own 128 GB compact flash cards stored the captured images; the card size was sufficient for the system to shoot continuously for about an hour, taking about 4500 images per camera in raw Canon format. A subset of some 10 300 images with minimal (< 10 %) or no overlap captured during six longer survey flights was selected for further processing and used in the presented study. To form this subset, every second image from one of the cameras was used. Figure 1 shows the selected flight tracks. Results of the data analysis from these flights together with in situ observations are reported below and also summarized in Table 1.

2.2 Image and navigation data processing

For a typical flight altitude of about 35 m over the sea ice, the camera lenses used in the setup provide a footprint of about 60 by 40 m. With the CCD geometry at its native resolution this corresponds to a pixel size on the ground of about 1 cm. For typical helicopter roll (pitch) angles of about −2°(1°) the distortion of the image plane from an ideal rectangular one and the associated uncertainty in the image area of less than 1 % was considered insignificant; therefore no correction for pitch and roll was applied to the images.

Image correction for camera lens distortion is necessary prior to any further analysis of the acquired images. We used a generic lens correction and vignetting correction procedures implemented in ®Adobe Lightroom software.

In order to discriminate between open water, bare ice, and melt ponds, we applied a three-step object identification and classification procedure. This involved:

a. image segmentation/binarization using Otsu's method, which chooses the threshold to minimize the intra-class variance of the black and white pixels (Otsu, 1979)

b. boundary tracing on the binarized images by the Moore-Neighbor tracing algorithm modified by Jacob's stopping criteria (Gonzalez, 2010)

TCD
8, 3699–3732, 2014

c. object classification (open water, bare ice or melt pond) using thresholding in the red channel intensity.

Due to the relatively high contrast between the different surface types during summer melt, this relatively simplistic approach appeared to work well with a minimum of supervision required during the processing of the sequences of images captured by the camera system. All procedures were implemented in Matlab using the "Image processing" toolbox (MATLAB, 2012).

Figure 2 demonstrates an example of the object classification procedure for an image captured during flight 1 (Table 1). The edges of the melt pond objects are accurately identified. Note that we left out the darker objects with an area less than 0.5 m^2, as the contribution of these objects to the total melt pond coverage was found to be negligible. The identified set of objects of three types is then used for calculating summary statistics on melt pond coverage and open water fraction. The parts of the image not classified as melt ponds or open water were considered as bare sea ice. For the case in Fig. 2 the open water fraction (f_{ow}) was calculated to be 8 % and the fractional melt pond coverage (f_{mp}) was 16 % with respect to the total sea-ice area.

2.3 Aggregate albedo

Hudson et al. (2013) used a different surface type classification technique from Renner et al. (2013) that additionally discriminated between two types of melt ponds on the sea ice surface: dark and bright ponds. The latter refers to light blue ponds with thicker, more reflective ice underneath. The broadband albedo of these three sea-ice surface types was measured in situ during the ICE12 drift experiment using a mobile instrument platform for measuring the radiation budget on sea ice (Hudson et al., 2012, 2013). In the estimates that follow we use the ratio of "dark" to "bright" pond areas, $r = 2.8$, determined from the additional analysis of 859 randomly selected images from flight 2 using the method of Renner et al. (2013). We also use the measured mean surface albedo of dark and bright ponds, $\overline{\alpha_{dp}} = 0.15$ and $\overline{\alpha_{bp}} = 0.34$, respectively, and of bare

TCD
8, 3699–3732, 2014

white ice $\overline{\alpha_{bi}} = 0.55$ (see Table 1 in Hudson et al., 2013 for more details and Supplement Table S1 presented here). The albedo of open water/leads is set to the commonly used $\overline{\alpha_{ow}} = 0.066$ (Pegau and Paulson, 2001). We note that cloudy conditions prevailed during the drift experiment, ensuring relative homogeneity in illumination in the study area.

The aggregate albedo is generally defined as (Perovich, 2005):

$$\alpha = g(\alpha_j, f_j) := \sum_j \alpha_j f_j; \{\alpha_j, f_j\} \in [0,1] \quad (1)$$

where summation is over all surface types used, here $j = \{\mathrm{ow}, \mathrm{bi}, \mathrm{bp}, \mathrm{dp}\}$, with the corresponding fractional coverage f_j. Note that for convenience we use the fractional total melt pond coverage f_{mp} with relation to the sea-ice area. Coefficients f_{bp} and f_{dp} are defined as fractions of bright and dark melt ponds with regard to the relative melt pond coverage, i.e. $f_{bp} = (1/(1+r))f_{mp}$ and $f_{dp} = (r/(1+r))f_{mp}$. This transforms Eq. (1) for α to

$$\alpha = \alpha_{ow} f_{ow} + \alpha_{bi}(1 - f_{mp})(1 - f_{ow}) + \alpha_{bp} f_{bp}(1 - f_{ow}) + \alpha_{dp} f_{dp}(1 - f_{ow}) \quad (2)$$

For example, the fractional melt pond coverage of $f_{mp} = 16\,\%$, with respect to sea ice area, and open water fraction of 4 % of the 0.95 km^2 of the ICE12 floe area yields an aggregate albedo of about 0.48.

In this study, the values of open-water and melt-pond fractions, the areal ratio of dark to bright ponds, and the average albedo of the main surface types are considered random variables. The probability densities of the quantities are estimated from the respective empirical distributions and presented below in Sect. 2.4.

TCD
8, 3699–3732, 2014

2.4 Accounting for uncertainties in the variables used

2.4.1 Error models for melt ponds and open water fractional coverage

Error models on the fractional coverage of open water and melt ponds are built on the additional analysis of 859 images from flight 2 using the classification method of Renner et al. (2013). The technique involves a semi-automated surface type classification and manual supervision of the processed images, allowing more reliable results at the cost of increased labour intensity. Processing of the images used in this verification procedure yielded the image-based fractional coverage of the four surface classes: dark ponds, bright ponds, open water or leads, and bare ice. This dataset was used as a reference to estimate the uncertainty in the corresponding quantities derived from the larger image set and to assess the probability density of the ratio of the areas of dark to bright ponds at the regional scale.

Imagewise intercomparison of f_{mp} and f_{ow} values demonstrated an average bias of $f^{\mathrm{b}} = 0.04$ with $\sigma_{f^{\mathrm{b}}} = 0.05$ in the fraction of melt ponds between the images processed using the technique of Renner et al. (2013) and the simplified approach applied in this study. Inspection of images revealed that the algorithm presented in Sect. 2.2 sometimes underestimates the melt pond coverage by identifying some bright ponds as bare white ice. Likewise, some of the darkest melt ponds were sometimes misidentified as open water/leads. The error model for f^i_{mp} and f^i_{ow} of an image i is therefore defined as

$$\left\{p\left(f^i_{\mathrm{mp}}\right), p\left(f^i_{\mathrm{ow}}\right)\right\} = \begin{cases} p\left(f^i_{\mathrm{mp}}\right) \sim p\left(f^i_{\mathrm{mp}} + \mathcal{N}\left(f^{\mathrm{b}}, \sigma^2_{f^{\mathrm{b}}}\right) \middle| \mathcal{N}\left(f^{\mathrm{b}}, \sigma^2_{f^{\mathrm{b}}}\right) \geq 0\right) \\ p\left(f^i_{\mathrm{ow}}\right) \sim p\left(f^i_{\mathrm{ow}} - (1 - f^i_{\mathrm{ow}})\mathcal{N}\left(f^{\mathrm{b}}, \sigma^2_{f^{\mathrm{b}}}\right) \middle| \mathcal{N}\left(f^{\mathrm{b}}, \sigma^2_{f^{\mathrm{b}}}\right) < 0\right) \end{cases} \quad (3)$$

where parameters of the Gaussian distribution were estimated from the data.

The areal ratio of dark to bright ponds r was estimated using a bootstrap technique (Efron and Tibshirani, 1993) involving sampling with replacement from the same complementary dataset of classified images, followed by a re-estimation of the sought r

TCD
8, 3699–3732, 2014

for each bootstrap replicate. The proportion of the drawn to replaced data points (i.e. classified images) within each replicate was set to 2/1 with all the images being equally weighted. The resulting distribution of the mean areal r derived from 10 000 replicates was approximated by a Gaussian probability density function with $p(r) \sim \mathcal{N}(2.8, 0.15^2)$.

2.4.2 In situ broadband albedo as a random variable

Uncertainties in the average in situ albedo $\overline{\alpha_j}$ are estimated empirically from available data for each surface type j. During the ICE12 experiment we obtained 50 individual albedo measurements over bare white ice, 12 over dark melt ponds, and 1 over a bright pond. This yields sample standard deviations $\sigma_\alpha^{\mathrm{sp}}$ on single point measurements of 0.05 and 0.04 for bare white ice and dark ponds, respectively (see Supplement Table S1 for details). Using a simplistic error model assuming independent measurements with random Gaussian errors, we calculate the uncertainty of the measurement-based average albedo of surface type j as

$$\sigma_{\overline{\alpha_j}} = \frac{\sigma_{\alpha_j}^{\mathrm{sp}}}{\sqrt{m_j}} + \frac{\sigma_{\alpha_j}^{\mathrm{ins}}}{\sqrt{m_j}} \tag{4}$$

where m_j refers to the number of available albedo measurements in the surface type under consideration. The single measurement instrumental error $\sigma_{\alpha_j}^{\mathrm{ins}}$ was set to $0.1\overline{\alpha_j}$, where the coefficient 0.1 stems from a declared 5 % measurement uncertainty yielding a total uncertainty of 10 % for the ratio of reflected to incoming radiation (i.e. albedo), again assuming the errors are independent. For the "bright pond" category, where only one albedo measurement was available with no significant influence from other surface types, we assigned an uncertainty of $0.1\overline{\alpha}_{\mathrm{bp}}$ although we acknowledge that this value can be a biased estimate. For the open water albedo uncertainty a value of 0.0066, derived from 24 measurements, was adopted from Pegau and Paulson (2001). Supplement Table S1 shows the resulting values of $\sigma_{\overline{\alpha_j}}$ for the four surface classes. The

TCD
8, 3699–3732, 2014

mean albedo of every surface type j can now be considered as a t distributed random variable with m_j degrees of freedom, distributed as $p(\overline{\alpha_j}) \sim \overline{\alpha_j} + t_{m_j}\sigma_{\overline{\alpha_j}}$. The use of t distribution accounts for a larger spread in the estimate of the true mean when dealing with the relatively small sample sizes. For bright ponds, the Gaussian approximation was used instead to prevent the occasional generation of albedo values outside the admissible range of $[0, 1]$ due to heavy tails of the t distribution with one degree of freedom.

This approach should be considered a simplification, as it reduces the whole variety of surface types with different optical chartacteristic to only four major surface types. However we expect that the imposed range of random variability in a particular surface-type albedo covers the natural variation of this parameter, thereby accounting indirectly for the effects of numerous additional factors like the thickness of ice, surface state and small scale morphology, pond depth and ice thickness beneath the pond as well as changing light conditions.

3 Results and discussion

3.1 Spatial variability of melt pond coverage and open water inferred from helicopter surveys

This section presents the results of the analysis of sea ice imagery along the six selected flights tracks that took place during the ICE12 cruise (Table 1). All but one flight (flight 1, on 31 July) were combined EM-bird/ICE camera flights, which fixed the helicopter flight altitude to approximately 35 m above the sea-ice surface, except for some shorter periods of climbing to 150–200 m for EM-bird calibration. During the calibration the helicoper typically hovered above the same location and only a few images captured during the calibrations were retained for the analysis.

Figures 3 and 4 show the summary statistics of melt pond and sea ice/open water fractions along the tracks of flights 2 and 6. The data for the other four flights are

TCD
8, 3699–3732, 2014

presented in Supplement Figs. S1, S3, S5, and S7. For five of six flights, those carried out from 31 July to 2 August, the results are similar, with a typical fractional melt pond coverage f_{mp} of about 25 % and a similarity in the shapes of the respective probability density distributions. The open water fraction f_{ow} varies between 7 and 13 %, but this variability lies within the uncertainty of the mean estimates and corresponds well to the respective operational ice charts for the area.

Flight 6, on 3 August, was conducted while moving southwards out of the close drift ice. The flight track traversed the marginal ice zone (MIZ) with extensive areas/strips of open water. Thus the estimates of f_{ow} (30 %) and f_{mp} (20 %) for flight 6 are substantially different from those inferred from survey flights conducted the previous days in the close pack ice (see Fig. 4).

3.2 Estimating regional albedo from in situ measurements and helicopter borne imagery

3.2.1 Bootstrapping to upscale the local albedo measurements to a regional scale

The results of in situ measurements from the ICE12 drift experiment are further upscaled to assess the regional scale albedo in the study area using the flight-track data of surface-type distribution, more specifically the series of $\{f^i_{mp}, f^i_{ow}, S^i\}$, $i = 1, \ldots, N$, with S^i standing for the respective area of image i. Figures 5a and 6a show local (i.e. based on individual images) aggregate albedo estimates α^i made from the helicopter imagery along the two selected flights with the contrasting surface conditions presented in Sect. 3.1. The results for other tracks are presented in Supplement and further summarized in Table 1. Note that in this case the image-based albedo variability is estimated from the data treated "as is" without taking the uncertainties into account.

Figure 5b and corresponding figures in the Supplement demonstrate fairly similar probability distributions of local aggregate surface albedo for the five similar flight tracks, suggesting a homogeneous state of sea ice cover in the area within approxi-

TCD
8, 3699–3732, 2014

mately 80 km of the ICE12 floe. We note that the empirical probability density functions (pdf) of local albedo are skewed substantially towards zero, due to the contribution of open water areas. This suggests that an estimate of the regional scale surface albedo of melting sea ice pack made by simple averaging of the respective quantities from a sequence of local scenes can be negatively biased. This may have implications for areal estimates of the surface energy budget, both in observational and modeling studies. Moreover, as in the case of any random variable with an a priori unknown theoretical distribution, the accuracy of the parameters of its empirical estimate is related to the availalbe data sample.

The whole swath-based aggregate albedo α^{s} is therefore calculated in the same way as the local estimates using Eq. (2), with the values of $f^{\mathrm{s}}_{\mathrm{ow}}$ and $f^{\mathrm{s}}_{\mathrm{mp}}$ derived as

$$f^{\mathrm{s}}_{\mathrm{ow}} = \sum_i S^i f^i_{\mathrm{ow}} \Big/ \sum_i S^i$$

$$f^{\mathrm{s}}_{\mathrm{mp}} = \sum_i S^i \left(1 - f^i_{\mathrm{ow}}\right) f^i_{\mathrm{mp}} \Big/ \sum_i S^i$$

and referring to the swath-based estimates of open water and melt pond fractions.

Since the probability distribution of the local, image-based albedo α^i, is non-Gaussian, the large number of available samples makes the bootstrapping (i.e. sampling with replacement) technique (Efron and Tibshirani, 1993) an optimal choice to assess the accuracy of the estimated swath albedo. The presence of autocorrelation in the data suggests the use of the moving block bootstrap approach (Kunsch, 1989).

For each flight the application of this method to the sequence of $\{f^i_{\mathrm{ow}}, f^i_{\mathrm{mp}}, S^i\}$ involves the following steps:

1. The series of $\{f^i_{\mathrm{ow}}, f^i_{\mathrm{mp}}, S^i\}$ of length N is split into $N - K + 1$ overlapping blocks of length K; the block length is determined empirically from the data, the procedure is described in the next subsection.

TCD
8, 3699–3732, 2014

2. N/K blocks are drawn at random, with replacement, from the constructed set of $N - K + 1$ blocks, and their sequence numbers are registered.

3. M bootstrap samples are drawn from the subset of N/K blocks; albedo for the four different surface types and the values for f^i_{ow}, f^i_{mp} and r can at this step be drawn at random from the respective probability distributions defined in Sects. 2.4.1 and 2.4.2; the swath-based albedo α^s is then calculated for each sample using Eq. (2).

Steps 2–3 are repeated L times to generate $L \cdot M$ estimates of the swath-based aggregate albedo α^s. The assigned values of $\{L, M\} = 200$ yield a total of 40 000 samples of α^s which is sufficient for minimizing the effect of random sampling errors. Panels c in Figs. 5, 6 and Supplement Figs. S2, S4, S6, S8 display the generated bootstrap probability density of the swath-based α^s for the six flights. The 95 % confidence interval ($CI_{0.95}$) on each estimated swath-based albedo is then calculated as $\{2.5, 97.5\}$ percentiles of the emprirical bootstrap pdf of α^s. Table 1 shows the calculated values of the average swath-based albedos and their respective bootstrap $CI_{0.95}$. For all tracks the α^s probality density is approximately Gaussian, with 95 % confidence according to the Lilliefors goodness-of-fit test of composite normality (Conover, 1999). The respective fits are shown together with the bootstrap pdfs in Figs. 5, 6 and Supplement Fig. S2, S4, S6 and S8. The standard deviations of the fitted Gaussian distributions are $\sigma_{\alpha^s} = 0.01$ for flights 1–5 and $\sigma_{\alpha^s_6} = 0.02$ for flight 6.

The five similar flight tracks demonstrate similar values of the swath-based aggregate albedo α^s, all lying within the estimated confidence intervals (see Fig. 7). This suggests the data from these five flights can be combined to provide the regional-scale estimate of the surface albedo. This is implemented using the same technique applied to the concatenated sequence of $\{f^i_{mp}, f^i_{ow}, S^i\}$ for all flight tracks but flight 6. The latter was not included in calculations of the regional estimate due to a substantially different state of sea ice cover, with implications for the estimated α^s_6. The results of calculations are presented in Fig. 7, and Table 1 further summarizes the results of the analysis.

TCD
8, 3699–3732, 2014

In order to infer the relative contribution of the spatial variability in melt pond/open water coverage and the uncertainty of in situ albedo measurements to the overall variance of the swath-based and regional albedo estimates, we repeated the numerical experiments, with the albedo of surface types treated as constants. The result demonstrated a substantial reduction in standard deviation of σ_{α^s} to 0.003 and σ_{α^r} to 0.002. This indicates that in the defined framework about 90 % of the estimated variance of α^s and 95 % in α^r is due to variability and uncertainties in the in situ albedo measurements. Only a minor part of the variance is due to all other errors and variability accounted for in the model.

3.2.2 Estimating the image block length K using the Markov chain

Accounting for the autocovariance in the analyzed data is implemented following the Nychka et al. (2000) modification of the Mitchell et al. (1966) formula

$$N_{\text{eff}} = N\frac{1-\phi-0.68/\sqrt{N}}{1+\phi+0.68/\sqrt{N}}, \tag{5}$$

where N_{eff} stands for the effective number of degrees of freedom ("effective sample size"); in general, $N_{\text{eff}} < N$ due to the presence of autocorrelation in a series. This approach implicitly assumes that the analyzed sequence can be adequately described as a realization of the discrete first order autoregressive process with the autoregressive parameter ϕ.

For each classified image i treated as an individual data sample, further categorization into "ice" or "open water" was applied. Such binarization into the two major surface classes is related to their dominant contribution to the swath-based albedo variance. The images within one flight track that have both open water and sea ice were categorized using a threshold in local open water fraction. The value for the threshold f^t_{ow} was set to 5 %, which for the typical flight altitude would correspond to an opening in sea ice cover at least a few meters wide, i.e. a very small fracture according to WMO sea-ice nomenclature (World Meteorological Organization, 1970).

TCD
8, 3699–3732, 2014

Fitting the Markov chain of first order to the derived binary sequence of surface states comprising one complete flight yields the transition matrix **T**. Its largest entry, which in our case characterizes the likelihood of retaining the "ice" state between two successive images, was used as the sought parameter ϕ – a simplistic metric of spatial autocorrelation in the surface state for the analyzed flight track. The resulting values of ϕ varied in the range of 0.78–0.88, whereas the probability of retaining the "open water" state was lower, 0.51–0.57. These results are summarized in Table 2. The block length K was then calculated as a ratio of N/N_{eff}, yielding a block size of 9–12 images for four of the six transects, which correspondeds to approximately 500–700 m of the flight track. For the tracks with the lowest (flight 1) and highest (flight 6) open water fractions the derived block lengths were 18 and 7 images, respectively.

3.2.3 Assessing the aggregate scale for ICE camera imagery

The notion of aggregate scale for an environmental variable refers to the minimal spatial scale at which the contribution of local sampling variability to its total variance is diminished (Moritz et al., 1993). The concept is directly related to the weak law of large numbers, provided that the samples are drawn from a stationary distribution. Knowledge of this scale is crucial for an accurate upscaling of local measurements and subsequently linking them to larger-scale climate models. We note that in a hierarchy of spatial scales the present study focuses specifically on the range of meters to hundreds of kilometers that encompasses the scales typical for in situ measurements up to regional and CGCM models.

The aggregate scale for the regional albedo was estimated using sets of (pseudo)-independent samples of different size drawn from the whole collection of classified images. The sample size varied from 10 to 1000 images, and for each sample size 10 000 subsets were drawn at random, without replacement, to gain the necessary statistics on the aggregate albedo distribution as a function of sample size and total sample area. As the image areas within each sample were not identical due to variations in the flight altitude, the average total area for each sample size was used. Images with an

TCD
8, 3699–3732, 2014

area over 6000 m^2, corresponding to a flight altitude above 55 m, were not included in the analysis.

Figure 8 (black lines) shows the fraction of sample-based aggregate albedo estimates falling within the interval of ±1 and ±2 standard deviations of the regional aggregate albedo (Table 1), as a function of sample area. The results demonstrate a rapid growth in the proportion of accurate estimates of the regional albedo with an increase in the number of images drawn for analysis. The curves level out when the total sample area exceeds the threshold of about 0.7 km^2, when some 95 % of the subset based estimates lie within the interval of 2 STD of the regional bootstrap albedo. One should emphasize that these estimates are specific to this study's setup, time period and region. For the range of flight altitudes typically sustained during the operation of the EM-bird, the 0.7 km^2 aggregate scale corresponds to a set of at least 300 independent images spatially representative of the study region.

In order to simulate higher flight altitudes and examine the effect of smaller sample sets and/or sub-kilometer scale spatial autocorrelation in the state of sea ice cover on the estimate of the aggregate scale, the numerical experiment was repeated with successive images combined into blocks of different length. The validity of this experiment relies on the assumption of smaller scale anisotropy in statistical properties of the sea ice surface. The red and gray lines in Fig. 8 show the fraction of the accurate estimates of the regional albedo for image blocks of length 10 and 25 images, respectively. Results suggest an increase in the aggregate scale to values above 2 km^2 which would correspond to sets of at least 80 (30) area-representative images captured from an altitude of about 100 (170) m. Notably the estimated thresholds (aggregate scales) have an order of magnitude similar to the respective estimate of about 1 km^2 obtained by Perovich et al. (2002) during the SHEBA experiment in a different region of the Arctic.

TCD
8, 3699–3732, 2014

4 Conclusions

The formation of smaller scale features such as melt ponds on summer sea ice entirely alters its optical properties over a broad range of wavelengths. This has implications for the surface energy balance and summer sea ice decay as well as for practical issues of the remote sensing of sea ice. The study of sea ice topography and associated processes at these smaller scales is therefore of crucial importance for a better understanding of the seasonal evolution of the ice pack at a pan-Arctic scale. Yet considerable regional and intraseasonal variability of summer first-year ice albedo stipulates the need for further regional scale studies of this parameter and its relation to other key physical factors characterizing the current state of sea ice cover.

Safety and logistical challenges associated with these types of studies result in the relevant field data preferentially representing thicker first-year sea ice at the initial stages of melt and/or sea ice from coastal areas, where the sediment load may modify the spectral albedo and melt pattern. Limited data exist for thinner, less than 1 m thick, Arctic first-year ice that is expected to occupy a substantial part of the Arctic basin in the future when (and if) the projected transition to a nearly seasonal ice cover has occurred.

Analysis of imagery from five of six low-altitude (35–40 m) ice survey flights during the ICE12 drift experiment north of Svalbard at 82.3° N in late July–early August 2012 revealed a regional scale homogeneity in melt pond coverage and open water fraction in the area of the drift track outside the MIZ. Within this area, with an extent of ≈ 150 km, the observed melt pond fraction varied from 15–36 % in 50 % of cases, around the mean of $f^i_{\mathrm{mp}} = 26\,\%$ relative to the sea ice area. In some occasions the melt ponds covered as much as 66 % of the ice surface, yet for some 10 % of images with sea ice in the field of view the sea ice surface exhibited no or very little melt pond coverage ($f^i_{\mathrm{mp}} < 4\,\%$). The average open water fraction of $f^i_{\mathrm{ow}} = 11\,\%$ was characteristic of very close drift ice and varied for the analyzed images between 0 and 8 % in 50 % of cases, with fewer than 1 % of images showing 100 % open water.

TCD
8, 3699–3732, 2014

As surface characteristics exhibit pronounced spatial variability at this range of scales, data inferred from individual low-altitude images must be considered as samples drawn from some random field with an a priori unknown distribution. Any result inferred from the entire dataset is therefore only an estimate, and the confidence interval on this estimate is to be provided. We used the block bootstrapping technique to account for uncertainties due to sampling in the spatial domain, surface type classification errors, and in situ albedo measurements used in the upscaling procedure. The set of more than 8000 classified images representing a total of 21 km^2, combined with a series of in situ broadband albedo measurements conducted on sea ice, was used to produce the regional aggregate albedo estimate of 0.40 (0.38; 0.42). The bootstrap albedo for flight 6, conducted within the MIZ, shows a lower value of 0.34 (0.31; 0.37) due to a higher open water fraction, 30 %. Notably the melt pond fraction of about 20 % observed during this flight was lower too. We speculate this is related to the smaller floe size and ice thickness in the MIZ promoting more efficient lateral drainage and percolation of melt ponds.

The use of a large collection of classified images from the area allowed an assessment of the aggregate scale for the regional albedo of about 0.7 km^2 which corresponds to at least 300 images captured by the ICE camera setup from an altitude of 35–40 m. Higher flight altitudes would require fewer classified images, though the area covered must be larger. We emphasize that these estimates are linked with the setup configuration used as well as the state of sea-ice cover during the ICE12 experiment.

The regional scale of this work and the relatively short time period covered complicate a comparison with similar studies on the topic. Analysis of the relevant literature indicates that our albedo estimates are systematically lower than the spatially averaged albedo of melting FYI reported in a number of other ship-based/aerial studies from matching latitudes and the time of year (Tschudi et al., 2001; Perovich et al., 2002; Perovich et al., 2009; Lu et al., 2010). The generally lower value of FYI albedo on a larger scale was found during the trans Arctic cruise ARK-XXVI/3 in 2011 (Nicolaus et al., 2012). The discrepancies can nevertheless be largely attributed to a substan-

TCD
8, 3699–3732, 2014

tial interannual/intraseasonal variability in surface conditions, including the prevalent ice type, melt pond and open water fractions, and the values of albedos for specific surface types used in upscaling to a regional aggregate estimate. A typical example is seen in the results of Lu et al. (2010), which report a much lower (less than 15 %) area fraction of melt ponds on sea ice observed along their cruise track in summer 2008. In the latitudes similar to our study this was however compensated by a much higher (> 40 %) open water fraction, yielding aggregate albedo estimates similar to this work. Higher ice concentrations, > 80 %, were observed farther north. The end of the melt season, associated with the onset of surface freeze up, however caused a low melt pond coverage (Lu et al., 2010) that kept the estimated albedo at a level higher than was esimated in this work. We note also that the current study was carried out on thinner sea ice, hence with darker melt ponds, which led to lower albedos for these two surface types and hence a lower regional albedo estimate compared with the similar values used in the aforementioned studies.

Our results indicate that about 95 % of the uncertainty in the regional albedo estimate as it was defined in our framework is due to variability in the in situ albedo measurements. This variability is related to both the natural local variability of this parameter due to, e.g. underlying ice thickness or pond depth, as well as the uncertainty stemming from the measurement technique itself. This indicates the need for a series of local measurements carried out for each surface category as a necessary prerequisite for a high quality regional uspcaling. A particular focus should be on melt pond albedo evolution at the latter stages of ice decay, when the ice beneath the ponds gets thin, the ponds begin to melt through, and their albedo approaches that of open water.

Further processing and analysis of the data from 2012 is an ongoing effort. The plans for further work include detailed analysis of the spatial melt pond distribution and a joint analysis of EM-bird ice thickness data, optical melt pond characteristics and ridging of sea ice. As the setup was designed to enable the capability of producing a 3-D reconstruction of the sea ice surface topography, some scenes will be selected for a detailed analysis of surface morphology.

TCD
8, 3699–3732, 2014

The Supplement related to this article is available online at doi:10.5194/tcd-8-3699-2014-supplement.

Acknowledgements. We thank the crew of R/V *Lance* and *Airlift* as well as other scientists and engineers on board for their assistance in carrying out the measurements. Funding was provided by the Centre for Ice, Climate and Ecosystems (ICE) at the Norwegian Polar Institute via the ICE-Fluxes project. This work was also supported by ACCESS, a European Project within the Ocean of Tomorrow call of the European Commission Seventh Framework Programme, grant 265863, and the Research Council of Norway through the EarthClim (207711/E10) project.

References

Conover, W.: Practical Nonparametric Statistics, Wiley Series in Probability and Statistics, 3rd Edn., Wiley, New York, 1999. 3712

Curry, J. A., Schramm, J. L., and Ebert, E. E.: Sea ice-albedo climate feedback mechanism, J. Climate, 8, 240–247, doi:10.1175/1520-0442(1995)008<0240:SIACFM>2.0.CO;2, 1995. 3701

Derksen, C., Piwowar, J., and LeDrew, E.: Sea-ice melt-pond fraction as determined from low level aerial photographs, Arctic Alpine Res., 29, 345–351, 1997. 3702

Doronin, Y. and Kheisin, D.: Sea Ice, Amerind Publishing Company, Office of Polar Programs and the National Science Foundation, Washington DC, 1977. 3701

Efron, B. and Tibshirani, R. J.: An Introduction to the Bootstrap, Chapman & Hall, New York, 1993. 3707, 3711

Gonzalez, R.: Digital Image Processing Using MATLAB, McGraw-Hill Education, India, Pvt Limited, 2010. 3704

Haas, C., Lobach, J., Hendricks, S., Rabenstein, L., and Pfaffling, A.: Helicopter-borne measurements of sea ice thickness, using a small and lightweight, digital EM system, J. Appl. Geophys., 67, 234–241, doi:10.1016/j.jappgeo.2008.05.005, 2009. 3703

Hohenegger, C., Alali, B., Steffen, K. R., Perovich, D. K., and Golden, K. M.: Transition in the fractal geometry of Arctic melt ponds, The Cryosphere, 6, 1157–1162, doi:10.5194/tc-6-1157-2012, 2012. 3701

TCD
8, 3699–3732, 2014

Holland, M. M., Bailey, D. A., Briegleb, B. P., Light, B., and Hunke, E.: Improved sea ice shortwave radiation physics in CCSM4: the impact of melt ponds and aerosols on arctic sea ice, J. Climate, 25, 1413–1430, doi:10.1175/JCLI-D-11-00078.1, 2012. 3701

Hudson, S. R., Granskog, M. A., Karlsen, T. I., and Fossan, K.: An integrated platform for observing the radiation budget of sea ice at different spatial scales, Cold Reg. Sci. Technol., 82, 14–20, doi:10.1016/j.coldregions.2012.05.002, 2012. 3705

Hudson, S. R., Granskog, M. A., Sundfjord, A., Randelhoff, A., Renner, A. H. H., and Divine, D. V.: Energy budget of first-year Arctic sea ice in advanced stages of melt, Geophys. Res. Lett., 40, 2679–2683, doi:10.1002/grl.50517, 2013. 3701, 3702, 3703, 3705, 3706

Karlsson, J. and Svensson, G.: Consequences of poor representation of Arctic sea-ice albedo and cloud-radiation interactions in the CMIP5 model ensemble, Geophys. Res. Lett., 40, 4374–4379, doi:10.1002/grl.50768, 2013. 3701

Kunsch, H. R.: The jackknife and the bootstrap for general stationary observations, Ann. Stat., 17, 1217–1241, doi:10.1214/aos/1176347265, 1989. 3711

Lu, P., Li, Z., Cheng, B., Lei, R., and Zhang, R.: Sea ice surface features in Arctic summer 2008: aerial observations, Remote Sens. Environ., 114, 693–699, doi:10.1016/j.rse.2009.11.009, 2010. 3717, 3718

MATLAB: Version 8.0.0.783 (R2012b), The MathWorks Inc., Natick, Massachusetts, 2012. 3705

Maykut, G.: Large-scale heat exchange and ice production in the Central Arctic, J. Geophys. Res., 87, 7971–7984, 1982. 3701

Mitchell, J., Dzerdzeevskii, B., and Flohn, H.: Climatic Change: Report of a Working Group of the Commission for Climatology, Technical Note 79, World Meteorological Organisation, 1966. 3713

Moritz, R. E., Curry, J., Thorndike, A., and Untersteiner, N.: SHEBA: A Research Program on the Surface Heat Budget of the Arctic Ocean, Report 3, Arctic Syst. Sci.: Ocean-Atmos.-Ice Interact., University of Washington, Seattle, 34 pp., 1993. 3714

Nazintsev, Y.: The heat balance of the surface of the multiyear ice cover in the central Arctic, Trudy AANII, 267, 110–126, 1964 (in Russian). 3701

Nicolaus, M., Katlein, C., Maslanik, J., and Hendricks, S.: Changes in Arctic sea ice result in increasing light transmittance and absorption, Geophys. Res. Lett., 39, L24501, doi:10.1029/2012GL053738, 2012. 3701, 3717

TCD
8, 3699–3732, 2014

Nychka, D., Buchberger, R., Wigley, T., Santer, B. D., Taylor, K. E., and Jones, R. H.: Confidence intervals for trend estimates with autocorrelated observations, available at: http://citeseerx.ist.psu.edu/viewdoc/download?doi=10.1.1.33.6828&rep=rep1&type=pdf (last access: 8 July 2014), unpublished manuscript, 2000. 3713

Otsu, N.: A threshold selection method from gray-level histograms, IEEE T. Syst. Man Cyb., 9, 62–66, doi:10.1109/TSMC.1979.4310076, 1979. 3704

Pegau, S. W. and Paulson, C. A.: The albedo of Arctic leads in summer, Ann. Glaciol., 33, 221–224, doi:10.3189/172756401781818833, 2001. 3706, 3708

Perovich, D. K.: On the aggregate-scale partitioning of solar radiation in Arctic sea ice during the Surface Heat Budget of the Arctic Ocean (SHEBA) field experiment, J. Geophys. Res.-Oceans, 110, C03002, doi:10.1029/2004JC002512, 2005. 3706

Perovich, D. K. and Polashenski, C.: Albedo evolution of seasonal Arctic sea ice, Geophys. Res. Lett., 39, L08501, doi:10.1029/2012GL051432, 2012. 3701

Perovich, D. K., Tucker, W. B., and Ligett, K. A.: Aerial observations of the evolution of ice surface conditions during summer, J. Geophys. Res.-Oceans, 107, 8048, doi:10.1029/2000JC000449, 2002. 3701, 3702, 3715, 3717

Perovich, D. K., Grenfell, T. C., Light, B., Elder, B. C., Harbeck, J., Polashenski, C., Tucker, W. B., and Stelmach, C.: Transpolar observations of the morphological properties of Arctic sea ice, J. Geophys. Res.-Oceans, 114, C00A04, doi:10.1029/2008JC004892, 2009. 3717

Petrich, C., Eicken, H., Polashenski, C. M., Sturm, M., Harbeck, J. P., Perovich, D. K., and Finnegan, D. C.: Snow dunes: a controlling factor of melt pond distribution on Arctic sea ice, J. Geophys. Res.-Oceans, 117, C09029, doi:10.1029/2012JC008192, 2012. 3702

Polashenski, C., Perovich, D., and Courville, Z.: The mechanisms of sea ice melt pond formation and evolution, J. Geophys. Res.-Oceans, 117, C01001, doi:10.1029/2011JC007231, 2012. 3701

Renner, A. H., Dumont, M., Beckers, J., Gerland, S., and Haas, C.: Improved characterisation of sea ice using simultaneous aerial photography and sea ice thickness measurements, Cold Reg. Sci. Technol., 92, 37–47, doi:10.1016/j.coldregions.2013.03.009, 2013. 3705, 3707

Tschudi, M. A., Curry, J. A., and Maslanik, J. A.: Airborne observations of summertime surface features and their effect on surface albedo during FIRE/SHEBA, J. Geophys. Res., 106, 15335, doi:10.1029/2000JD900275, 2001. 3717

Untersteiner, N.: On the mass and heat budget of arctic sea ice, Arch. Meteor. Geophy. A, 12, 151–182, doi:10.1007/BF02247491, 1961. 3701

TCD
8, 3699–3732, 2014

World Meteorological Organization: WMO Sea-Ice Nomenclature, Terminology, Codes and Illustrated Glossary, 1970 Edn., Secretariat of the World Meteorological Organization, Geneva, 1970. 3713
Zubov, N.: Arctic Ice, Izd. Glavsevmorputi, Moscow, 1945 (translated by US Navy Oceanographic Office, Springfield, 1963). 3701

TCD
8, 3699–3732, 2014

Table 1. Summary statistics on the state of sea ice cover and aggregate surface albedo along the six processed helicopter flight tracks from ICE12 cruise. The open water coverage f^s_{ow}, melt pond fraction f^s_{mp} (relative to sea ice area) and albedo values presented are the whole swath-based estimates rather than averages of the respective values from individual images presented in the corresponding figures. The regional aggregate scale albedo is calculated in the same way from the whole dataset less flight 6. The numbers in parentheses in the albedo column denote the respective block bootstrap 95 % confidence interval on the estimates.

Flight number	Date	GMT start-end times	*N* images	Transect length (area), km (km^2)	f^s_{ow}, %	f^s_{mp}, %	Aggregate albedo (α^s)
1	31 Jul 2012	7:36–8:10	1031	67 (2.4)	7	26	0.41 (0.39; 0.44)
2	1 Aug 2012	7:22–8:34	1902	139 (5.0)	10	24	0.41 (0.39; 0.43)
3	1 Aug 2012	16:45–18:03	2237	154 (5.7)	14	25	0.39 (0.37; 0.41)
4	2 Aug 2012	11:21–12:00	993	78 (2.5)	14	24	0.40 (0.37; 0.42)
5	2 Aug 2012	13:21–14:45	2121	170 (5.2)	12	26	0.40 (0.38; 0.42)
reg. aggreg.	–	–	8284	608 (20.8)	12	25	0.40 (0.38; 0.42)
6	3 Aug 2012	14:43–16:04	1979	165 (7.4)	30	20	0.34 (0.31; 0.37)

TCD
8, 3699–3732, 2014

Table 2. Auxiliary data for the processed flight tracks used in calculation of the flight track albedo. T_{11} and T_{21} denote elements of the transition matrix of the fitted first order Markov model and the respective estimated image block lengths.

Flight number	T_{11} $\phi_{\text{ice}\to\text{ice}}$	T_{21} $\phi_{\text{ow}\to\text{ow}}$	block length
1	0.88	0.57	18
2	0.83	0.53	12
3	0.78	0.48	8
4	0.80	0.49	9
5	0.82	0.52	10
reg. aggreg.	0.82	0.51	10
6	0.76	0.25	7

TCD
8, 3699–3732, 2014

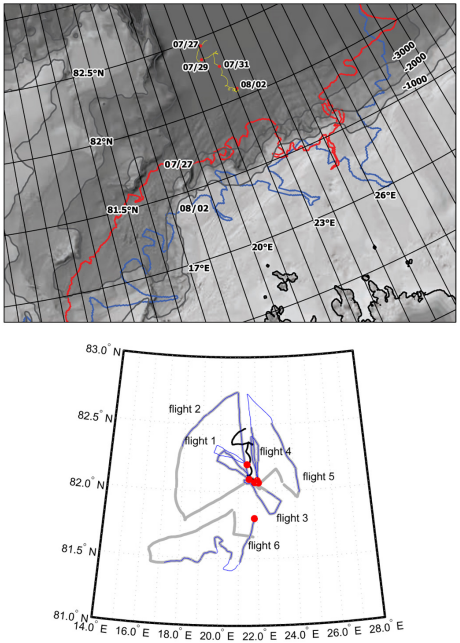

Figure 1. Upper panel: drift track of ICE12 floe during the study (yellow line); red dots mark locations at noon on the given dates. Bathymetry is shown in the grayscale background, with contours at 1000 m intervals. The red and blue curves show the ice edge on two days, on 27 July and 2 August, defined as 40 % ice concentration, based on ice charts from the Norwegian Meteorological Institute. Lower panel: tracks of the ICE12 floe drift north of Svalbard 26 July to 3 August 2012 (black) and six helicopter ice reconnaissance flight tracks (see Table 1). The grey and blue lines show the segments of the flight tracks with EM-bird and ICE camera data, respectively. Red dots mark the starting points for the flights. The data summary on the state of sea ice cover inferred from the ICE camera system for these flights is presented in Sects. 3.2 and 3.2.1

TCD
8, 3699–3732, 2014

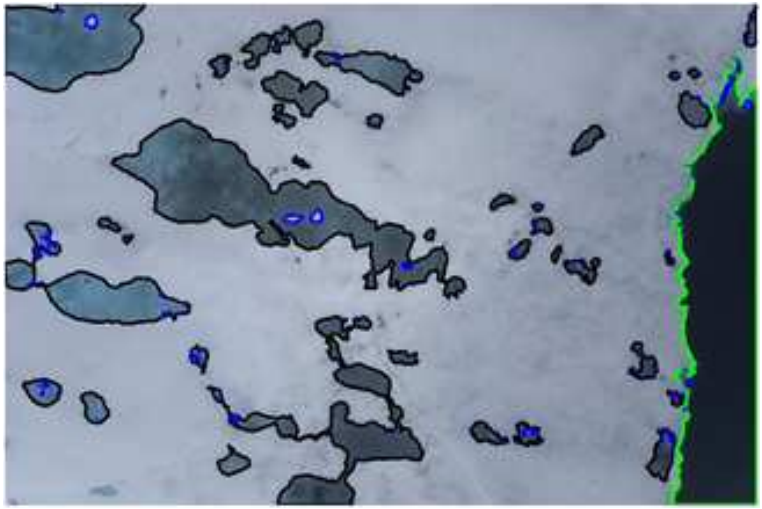

Figure 2. Example of the image segmentation procedure showing an image captured during flight 1 from an altitude of 35 m. The dimensions of the scene are 60.5 by 40.5 m. Black contours highlight the edges of melt ponds; the green contour outlines the open water area; blue is for the smaller patches of sea ice within melt pond/open water objects. For this particular scene the melt pond fraction f_{mp} (relative to sea-ice area) and open water fraction are 16 and 8 %, respectively.

TCD
8, 3699–3732, 2014

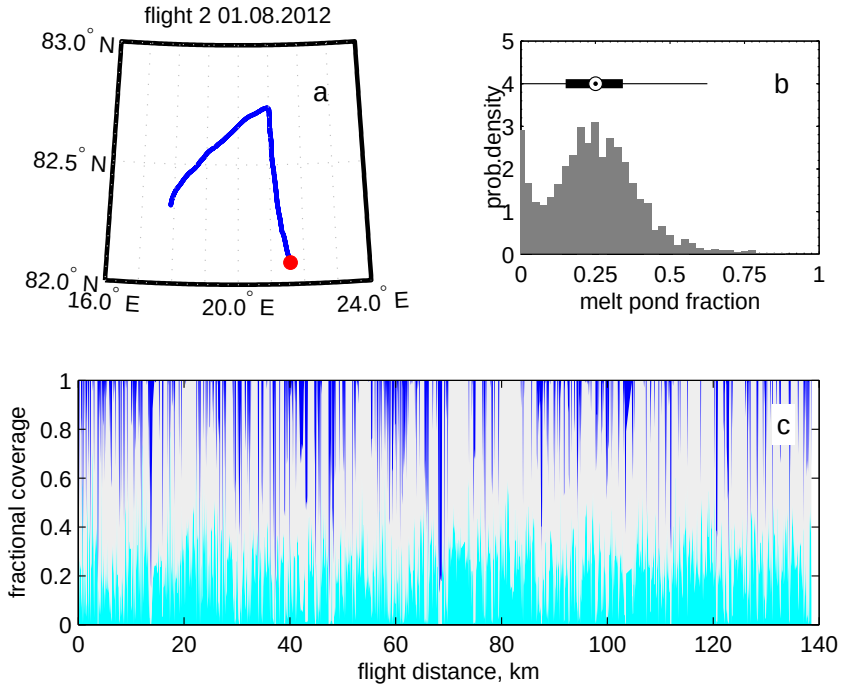

Figure 3. Data summary from flight 2 on 1 August 2012, 07:23–08:35 UTC; **(a)** flight track with photo coverage; **(b)** empirical probability density of fractional melt pond coverage f_{mp} along the flight track relative to sea ice; image-based mean f_{mp} of 25 % and the quartiles $Q_{1,2,3}$ of 15, 25 and 34 %, respectively, as shown by the Box plot; image averaged f_{ow} 9 %. The whiskers on Box plot highlight the 1.5 times interquartile range to cover some 99 % of the observations in total; **(c)** fractional melt pond coverage f_{mp} (light blue), bare ice f_{bi} (light grey) and open water fraction f_{ow} (blue) along the flight track relative to the image area. With a swath width of 35–40 m, the covered area corresponds to roughly 0.35–0.40 km^2 per 10 km flight track.

TCD
8, 3699–3732, 2014

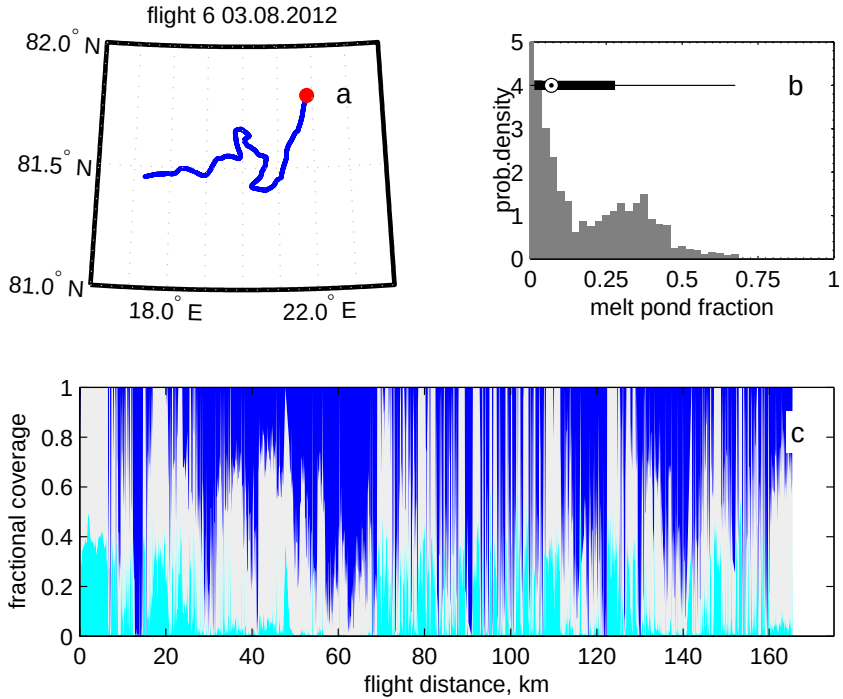

Figure 4. Same as in Fig. 3 but for flight 6 carried out in the MIZ on 3 August 2012, 14:43–16:04 UTC. Image-based mean f_{mp} of 15 % and the quartiles $Q_{1,2,3}$ of 1, 7 and 28 %, respectively, as shown by the Box plot; image averaged f_{ow} 37 %.

TCD
8, 3699–3732, 2014

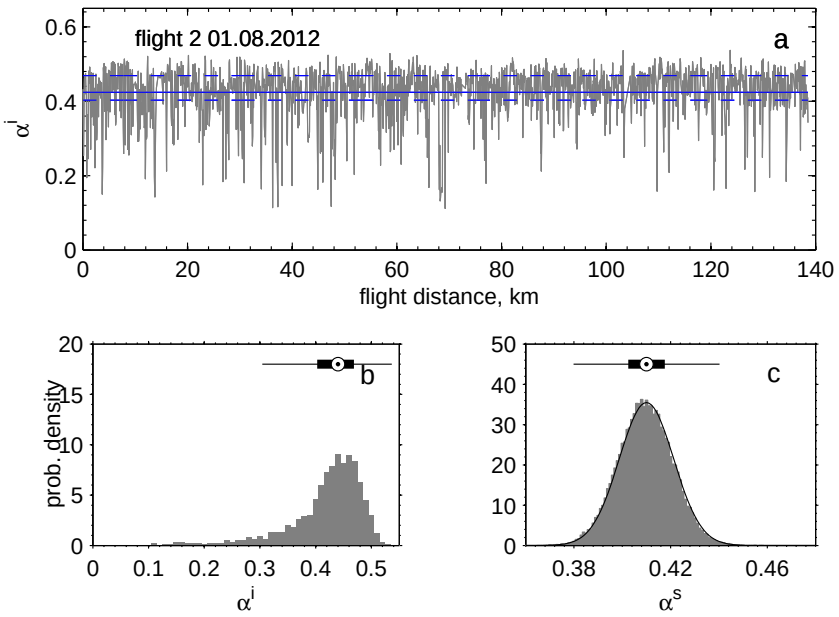

Figure 5. (a) Image-based aggregate surface albedo (α^i) along flight 2 track shown in Fig. 3. Solid blue line is for the image-based track average albedo of 0.42, dashed lines show the quartiles $Q_{1,3}$ of (0.40,0.47) of the respective α^i probability density shown in **(b)**. Note skewness of the distribution towards lower albedo values and asymmetric position of the mean with respect to the 25 and 75 percentiles; **(c)** bootstrap swath-based aggregate albedo α^s probability density, solid line shows the fitted normal pdf $\mathcal{N}(0.41, 0.01^2)$. The Box plots on **(b)** and **(c)** panels use the same conventions as in Fig. 3.

TCD
8, 3699–3732, 2014

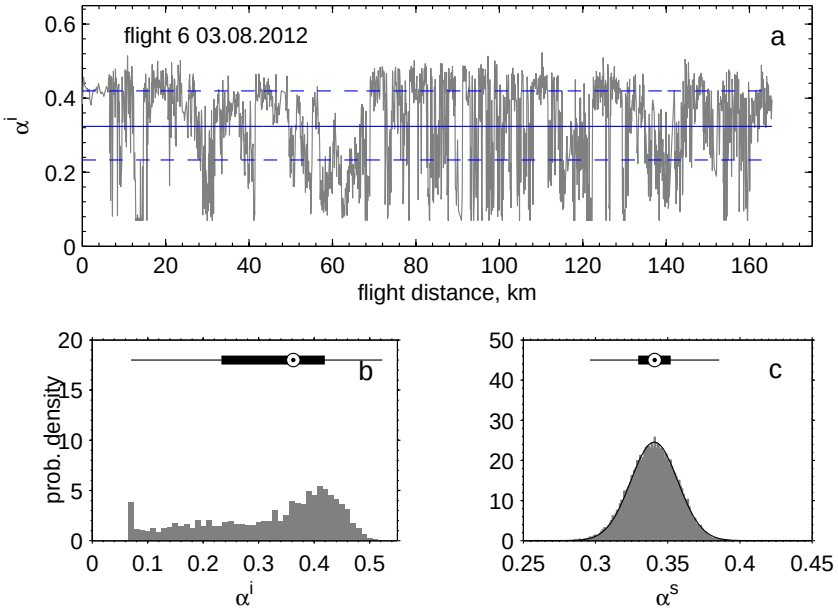

Figure 6. Same as in Fig. 5 but for flight 6 shown in Fig. 4. Solid blue line is for the image-based track average albedo of 0.32, dashed lines show the 25 and 75 percentiles (0.23,0.42) of the respective α^i probability density shown in **(b)**; **(c)** bootstrap swath-based aggregate albedo α^s probability density, solid line shows the fitted normal pdf $\mathcal{N}(0.34, 0.02^2)$.

TCD
8, 3699–3732, 2014

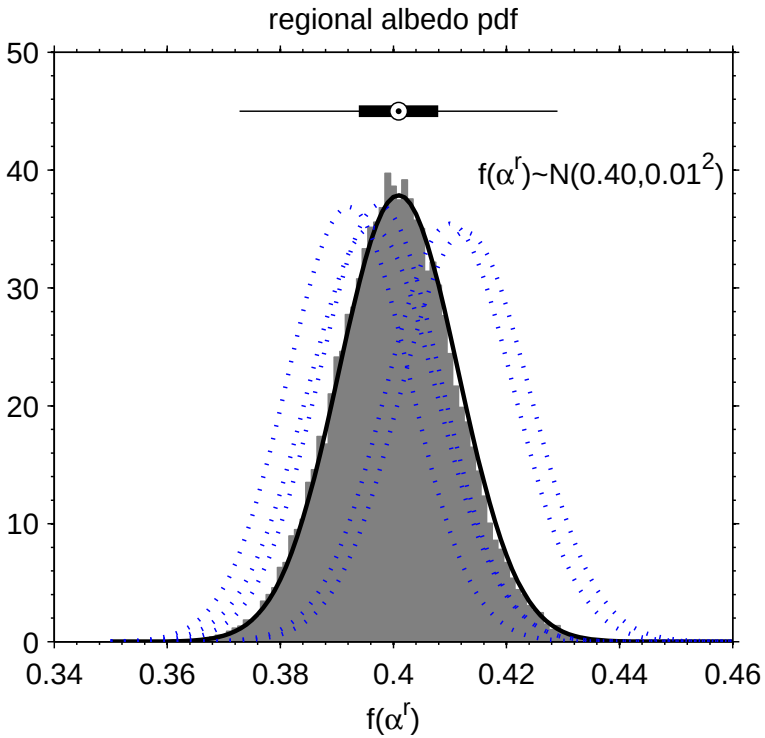

Figure 7. Regional albedo bootstrap probability density obtained from merging the data from flights 1–5. Solid black line highlights the fitted Gaussian pdf with the parameters indicated in the panel. Dotted blue lines show for the reference the fitted Gaussian pdfs for α^s from flights 1–5. The Box plot on the top of the panel uses the same conventions as in Fig. 3.

TCD
8, 3699–3732, 2014

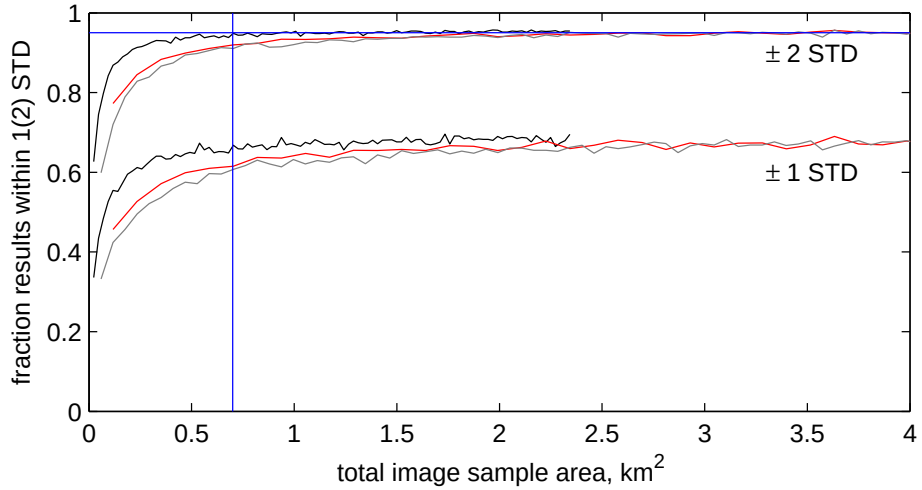

Figure 8. Fraction of image subset-based aggregate albedo values within the interval of ±1 and ±2 STD of the bootstrap estimated regional albedo as a function of total image (sample) area. The subsets are formed of image blocks of length 1 (black), 10 (red) and 25 (grey line) images. The solid blue lines highlight the 0.95 fraction and 0.7 km^2 aggregate scale for subsets formed of single image blocks.

TCD
8, 3699–3732, 2014